TUMSAT-OACIS Repository - Tokyo

University of Marine Science and Technology

(東京海洋大学)

Development of an instantaneous
velocity-vector-profile method using conventional
ultrasonic transducers

Development of an Instantaneous Velocity-Vector-Profile Method Using Conventional Ultrasonic Transducers

Dongik Yoon[a*], Hyun Jin Park[a], Tomonori Ihara[b]

[a]: Laboratory for Flow Control, Graduate school of Engineering, Hokkaido University
N13 W8, Kita-ku, Sapporo 060-8628, Japan

[b]: Department of Marine Electronics and Mechanical Engineering, Tokyo University of Marine Science and Technology, 2-1-6 Etchujima, Koto, Tokyo 135-8533, Japan

E-mail: yoon@ring-me.eng.hokudai.ac.jp

Abstract

The velocity vector profile technique based on an ultrasound pulsed Doppler method can enrich the information of a flow field, however, it has shown a low availability because a new design of special transducers is required for each measurement case. This study proposes a new method of profiling the velocity vectors using conventional ultrasound transducers that are widely supplied to UVP (Ultrasound velocity profile) users. We constructed a configuration of the transducers to minimize the uncertainty of the detection points at the receivers, and a measurable distance was theoretically determined by the configuration. Two feasibility tests were carried out. One was a test for the assessment of the measurable distance, which agreed well with the theoretical distance. The other was the evaluation of the measurement of two-dimensional velocity vectors by the new method and it was performed in a towing tank facility without the velocity fluctuation. From the evaluation, it was confirmed that the measured vectors showed good agreement to the reference values, and their accuracy and precision were competitive compared to previous studies. The developed method was applied to two unsteady flows for demonstrations. The results clarified that the proposed method guarantees high availability and accuracy for the velocity vector profiles.

Keywords: Ultrasound velocity profile, 2D velocity vector, Instantaneous vector, Conventional transducers, Unsteady flow

1. Introduction

Ultrasonic velocity profiling (UVP) became one of the powerful measurement tools used in hydrodynamics after Takeda started to apply this technique to fluid measurement [1]. It is applicable to the opaque flow without intrusions in the flow fields. Therefore, this technique has been adopted in various fluid measurement fields, such as liquid metal flow, flow rate measurement, and the inner structure of fruits [2–5]. Additionally, as the echo intensity reflected by a medium relies on the acoustic impedance of such a medium, the fluid phases based on the intensity can be determined [6]. For this reason, the UVP is also being widely utilized in multiphase flow studies [7–13]. In this measurement, a transducer works as not only an emitter but also a receiver, and it provides streamwise velocity vector profiles. To perform the measurement, first, we should select specifications of the transducer; the basic frequency and the sensor diameter. The basic frequency is

selected which is suited to the purpose of the measurement. Generally speaking, higher frequency is recommended for experiments requiring higher spatial resolution whereas lower frequency is preferred for experiments requiring longer measurement distance. The sensor diameter affects the ultrasonic beam diameter and the measurement volume. It is basically recommended to use a smaller diameter for improving the spatial resolution while a transducer with a too-small diameter cannot generate an ultrasonic beam field. Therefore, the appropriate sensor diameter of transducers is optimized by the basic frequency of the UVP measurement. For example, the diameters of 2 MHz, 4 MHz and 8 MHz transducer are generally 10 mm, 5 mm and 2.5 mm, respectively. We define those transducers as "conventional transducers" in this study. These specifications typically satisfy the requirements of the normal measurement field in water. Transducers with these specifications are, therefore, readily available on the market, and have been widely chosen by UVP users. An important limitation is that the UVP measurement with a conventional transducer setup can provide only one of the velocity components on a measurement line. This results in two issues: (1) Multiple-vector flow field cannot be measured with the conventional setup. (2) The instantaneous velocity profiles measured by one transducer are likely to include non-negligible errors other than a laminar flow because the UVP assumes that only one vector component exists in the flow. Since many industry fields require flow data such as Reynolds stress and vorticity, the UVP is not vigorously adopted in the fields. Many studies have been conducted to obtain multiple-vector information using the UVP in an attempt to overcome this limitation.

With regard to studies concerning two-vector profiling using the UVP called the vector-UVP (Table 1), Lemmin et al. suggested a three-vector measurement system with four tilted receivers and one emitter [14]. In this study, a focusing transducer was used as the emitter to reduce the spatial uncertainties of the measurement point. Obayashi et al. also developed a two-dimensional velocity profiling method using a focusing transducer together with a tilted receiver [15], and unsteady flow was measured using this method. A larger error was found in the velocity measured with a receiver because the echo intensity of side scattering is weaker than that of backscattering. In consideration of this, a phased array transducer was proposed and utilized in the measurement of the bubbly flow in a water tank and a recirculating flow in a bent pipe [16, 17]. Because beam steering is performed by element sequence, the phased array setup requires a specific scanning time for the measurement plane. As a result, time resolution can be worse in this measurement system. Furthermore, the phased array sensor makes the measurement system more complex. Meanwhile, Owen et al. developed an array transducer that had two horizontal elements ultrasonic transducer with both elements acting as transmitter and receiver [18] and calculated that the flow rate showed good agreement with an electromagnetic flowmeter. Additionally, they proposed a new type of element arrangement that included a center transmitter and side receivers [19]. A remarkable feature of these transducers was that they were equipped with very thin receivers (approximately a wavelength of a signal) to minimize the uncertainty concerning the detecting point at the receivers. Similarly, two vectors of the bubbly flow were acquired using a transmitter and two thin receivers [20], and the measured velocities of the liquid and the bubbles were in agreement with the particle image velocimetry (PIV) result.

Table 1. Previous studies regarding vector-UVP.

Year	Investigators	Used Transducers (TDX)	Incident Dimensions	Vector Dimensions	TDX Element Configurations
1998	Lemmin et al. [14]	Focusing TDX	1	3	Tilted element
2008	Ohbayashi et al. [15]	Focusing TDX	1	2	Tilted element
2017	Batsaikhan et al. [16]	Phased array TDX	2	2	Sectorial element array
2018	Shwin et al. [17]	Phased array TDX	2	2	Plane element array
2018	Owen et al. [18]	Element array TDX	1	2	Horizontal element
2018	Owen et al. [19]	Element array TDX	1	3	Horizontal element
2020	Wongsaroj et al. [20]	Thin receiver	1	2	Horizontal element

Concerning the above-described vector-UVP studies, special transducers were essential to gain the multiple vectors on the measurement line. As previously explained, large errors were caused in the receiver with the focusing transducer, and the reduction of the time resolution and complicated configuration of the measurement were inevitable using phased array transducers [14–17]. In the case of the array transducers, the emitter and the receiver should be made into one transducer body. However, the design of a special transducer is required for each measurement case, which lacks versatility in practical usage. These issues remain for thin receivers [20]. In fact, it can be said that the vector-UVP exhibits lower availability than the UVP even though it can offer more informative data than the conventional UVP setup. If the conventional transducers can be used for the vector-UVP, obviously, it will provide the high availability of the vector-UVP for the UVP users who already own the conventional transducers. In addition, by using the conventional transducers, the initial introduction cost of the vector-UVP will be reduced and it will make the entry of new users much simpler. For these reasons, our motivation of this study is to develop the vector profiling method using the conventional transducers accordingly. The conventional transducers have entailed uncertainty for acoustic distribution on a receiver surface, which makes the estimation of a detection point difficult. The detection point on the receiver is determined by opening angles between emitted line and reflected line at each measurement point. Moreover, the angles greatly affect the estimation of velocity vectors. A precise estimation of detecting points on the receiver should be a key prerequisite to obtain the velocity vector using the transducers. The present study investigates this issue and proposes a new instantaneous vector-profiling method using the conventional transducers. The principles of the proposed method are discussed in Section 2. The feasibility tests were completed using the proposed method in Section 3. Section 4 covers two demonstration experiment cases since we aimed to measure unsteady flows with the developed vector-UVP. First case is Reynolds stress measurement in a turbulent pipe flow, and the second case is an evaluation of vortex shedding flow behind a cylinder.
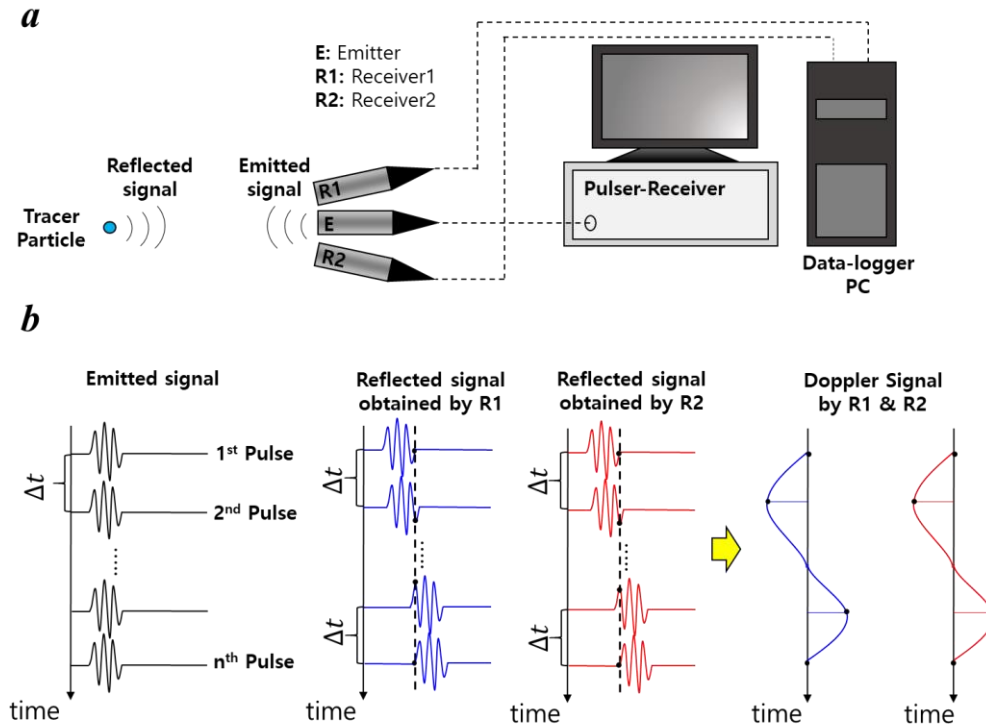
2. Measurement principle

Fig. 1. Schematics of the vector-UVP system. (a) A measurement system and (b) Doppler signal detection.

Multiple transducer elements are required to reconstruct velocity vectors on the vector-UVP so that they can provide multidirectional Doppler signals. Thus, in this study, three transducers were used: a central transducer played the role of an emitter, and side transducers played the roles of receivers, as shown in Fig. 1 (a). The emitter was driven by a pulser/receiver, and the ultrasound was emitted with a periodic interval ($\Delta t = 1/f_{PRF}$), as shown in Fig. 1 (b). The ultrasound signal reflected by the tracer particles was received by the side transducers and transmitted to a data logger. The detailed configuration of the transducers will be discussed in Sections 2.1 and 2.2. The transmitted signals were recorded on the memory of a PC, and their example is shown in Fig. 1 (b). Signal processing is essential to convert the echo signal to the flow velocity. Accordingly, quadrature phase demodulation [21] and the autocorrelation method [22] were used in this study.

As for the adoption of the conventional transducer, since 1 MHz to 8 MHz transducers are widely used in research and industry fields [2–5], we selected a 4 MHz transducer which is mid-frequency of the range. Note that the proposed method is applicable to the other transducers of different frequencies because the active diameter of them slightly is changed by each frequency. As the 4 MHz conventional transducer, we adopted the TX4-5-8-40 (Met-Flow S.A.) that has been widely used by UVP users as both emitter and receivers. The specifications of the transducer are summarized in Table 2.

Table 2. Specifications of TX4-5-8-40.

Basic frequency	Active diameter	Overall diameter	Near-field distance	Divergence half-angle
4 MHz	5 mm	8 mm	16.9 mm	2.2°

4

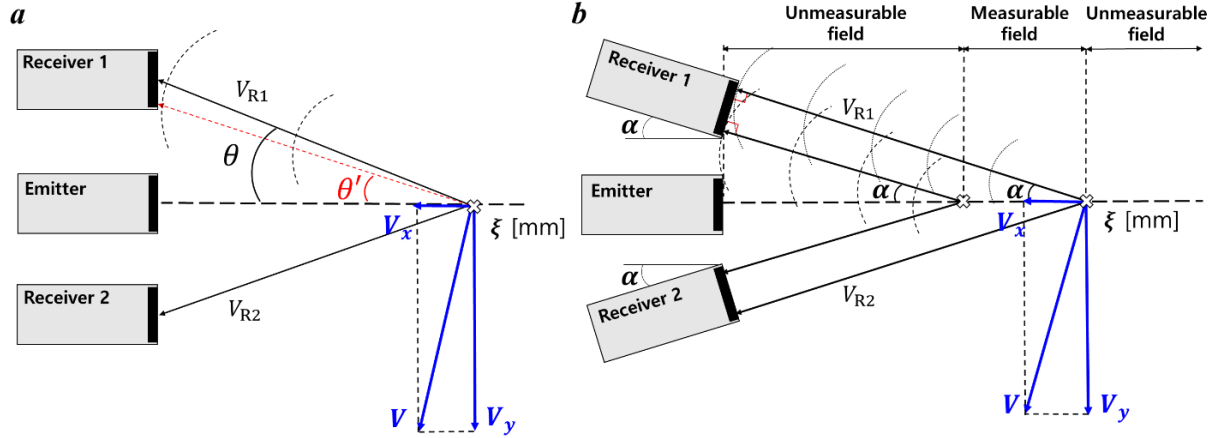## 2.1 Configuration of the transducer

Fig. 2. Transducer configurations. (a) The problem of the uncertainty of the detecting points at the receiver in the parallel transducer array and (b) the determination of the detecting point of the receivers with the tilting receiver.

The general transducer configurations in the vector-UVP are illustrated in Fig. 2, where V_x is a radial velocity, and V_y is an axial velocity regarding the emitter beam line. The configurations can be classified into two different types. One type consists of a central emitter and multiple side receivers, which are parallel to the emitter as shown in Fig. 2 (a), and this parallel array of emitter and receivers has been adopted in most vector-UVP studies (cf. researches using sectorial and plane element array or horizontal element in Table 1). One problem of this configuration is that it is difficult to evaluate the detecting point on each receiver because the sensor diameter (i.e., active diameter) of a conventional transducer is quite large (5 mm for the above-mentioned transducer) compared with the distance of the emitter and receiver transducers, which is somewhat restricted by an acoustic sensible area and cannot be set to be very far. As a result, the angle between the emitted line and the received line (θ) can vary significantly along the measurement line when it is assumed that the echo signal is always detected at the center points of each receiver. For example, the angle between the emitted and reflected lines can be considered θ with the assumption even though the actual angle is θ', as shown in Fig. 2 (a). This is due to the acoustic distributions for both emitter and receivers. Because the angle is one of the main parameters in the vector-UVP equations expressed in Eq. (1) [17], where c is the speed of sound and f_{R1} and f_{R2} are the Doppler frequencies measured by each receiver, this uncertainty causes errors for the calculation of two vectors. For this reason, previous studies [19, 20] used a 0.3-mm-thin receiver to minimize uncertainty, and this meant that it was very difficult to acquire two vectors with the conventional transducers in this configuration. The other problem of the parallel transducer array configuration is that measurements at the side receivers result in a lower SNR because the echo intensity of side scattering is weaker than that of backscattering. Thus, an opening angle is required at the receivers to minimize the SNR, as shown in Fig. 2 (b), and the effective opening angle varies on the measurement distance. Simultaneously, the angle between the emitted line and the received line should be corrected because the detection point at the receivers can also be varied by the measurement distance.

$$V_x = \frac{c(f_{R1}+f_{R2})}{2f_0(1+\cos\theta)} = \frac{V_{R1}+V_{R2}}{1+\cos\theta}, \quad V_y = \frac{c(f_{R1}-f_{R2})}{2f_0\sin\theta} = \frac{V_{R1}-V_{R2}}{\sin\theta}. \tag{1}$$

The other type of configuration, as shown in Fig. 2 (b), is composed of a central emitter and side multiple receivers with an inclined angle. It is possible to know the detecting point at the tilted receivers if it is assumed that the echo signal is sensed by the nearest point of the receivers from the

reflected point by a medium, as shown in Fig. 2 (b). Then, the reflected lines are perpendicular to the receiver's surface, and the angles between the measurement line and each reflected line become α, the same as the tilted angle of the receivers. Successively, the vector-UVP equation, Eq. (1), can be replaced with Eq. (2), using α and not θ.

$$V_x = \frac{c(f_{R1} + f_{R2})}{2f_0(1 + \cos\alpha)} = \frac{V_{R1} + V_{R2}}{1 + \cos\alpha}, \quad V_y = \frac{c(f_{R1} - f_{R2})}{2f_0\sin\alpha} = \frac{V_{R1} - V_{R2}}{\sin\alpha}. \tag{2}$$

A measurable field can be assumed based on the transducer diameter, the tilted angle of the receiver (α) and the distance between the emitter and each receiver as illustrated in Fig. 2 (b). This configuration has been mainly adopted in the use of focusing transducer (cf. researches with tilted element in Table 1) while this present study focuses on the employment of the conventional transducers. One of the advantages for conventional transducer employment is that measurable field can be adjusted by changing the transducer arrangement while a focusing transducer requires new fabrication of optimized transducer(s) according to the measurement target. The specific information for the measurable distance of the proposed system will be discussed more specifically in the next section.

2.2 *Measurable distances depending on the transducer diameters*
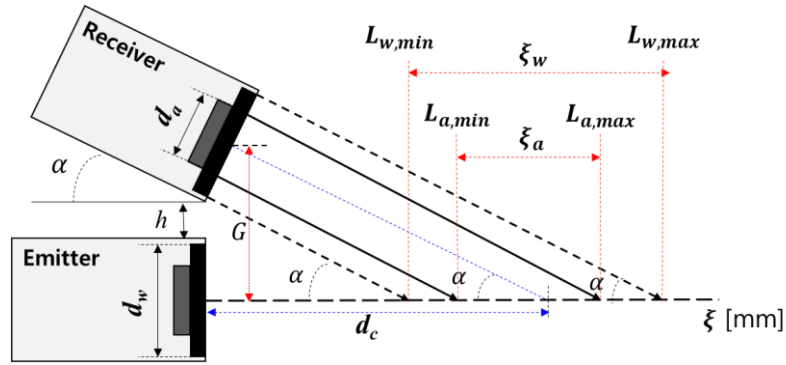
(a) Measurable distance calculated by the active diameter and the whole diameter of the transducer
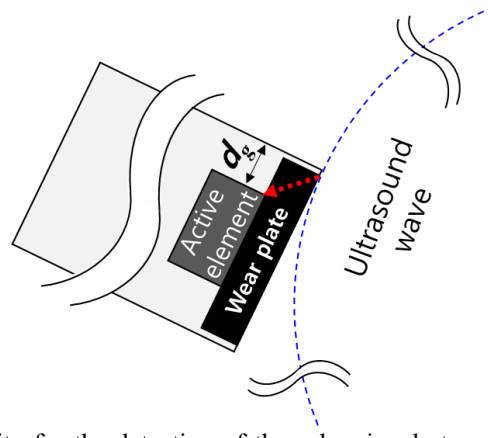
(b) Probability for the detection of the echo signal at a receiver surface other than the active element areas

**Fig. 3**. Measurable distance of the vector-UVP.

As shown in Fig. 3 (a), it is possible to estimate the measurable distance (ξ_a) based on the active diameter of the transducer (d_a) because the ultrasound beam is sensed at the active element. Furthermore, the start ($L_{a,min}$) and end ($L_{a,max}$) points of ξ_a are calculated by considering α and d_a. By contrast, the active diameter of the conventional transducer (TX4-5-8-40) is 5 mm, and the entire diameter (d_w) is 8 mm. Then, the gap between the two outer diameters (d_g) becomes 1.5 mm, as shown in Fig. 3 (b). As the gap is quite short, it is likely that the ultrasound detected at areas other than d_a is transferred by oscillating a wear plate. Considering this, another measurable distance (ξ_w) can also be considered based on d_w, and it has a wider range of measurement distance than ξ_a. However, the distances (d_c) between an emitter and a central point for ξ_a and ξ_w are equal because they are related in a concentric circle. We evaluated the measurable distances by comparing ξ_a and ξ_w to confirm whether ξ_w was acceptable or not in this transducer configuration.

Regarding the distance between the center points of the emitter and the receiver (G in Fig. 3 (a)), it was confirmed by Wongsaroj et al. [20] that the optimum G exists between 7 and 15 mm, and they selected 11 mm as the value for G. On the contrary, d_c also increases with the increase of h in the configuration of the transducer, and $L_{a,max}$ and $L_{w,max}$ are located distant from the emitter. As the echo intensity becomes weak by the measurement distance [23], the low SNR can be included when the measurement points approach $L_{a,max}$ and $L_{w,max}$. For this reason, we tried to minimize the gap between the emitter and receiver (h), and it was 1 mm, having a G of approximately 9 mm. Regarding α, three angles were adopted: 5°, 10°, and 15°. With these angles, the measurable distances were calculated, as summarized in Table 3.

Table 3. Geometric information regarding transducer configuration changed by receiver angles.

	$\alpha = 5°$	$\alpha = 10°$	$\alpha = 15°$
G [mm]	8.98	8.94	8.86
$L_{a,min}$ [mm]	74.2	37.0	24.5
$L_{a,max}$ [mm]	131.8	65.8	43.8
$L_{w,min}$ [mm]	57.2	28.4	18.7
$L_{w,max}$ [mm]	149.0	74.4	49.6
d_c [mm]	103.0	51.4	34.1
ξ_a [mm]	57.6	31.8	19.3
ξ_w [mm]	91.8	46.1	30.9

3. Evaluations of the vector-UVP
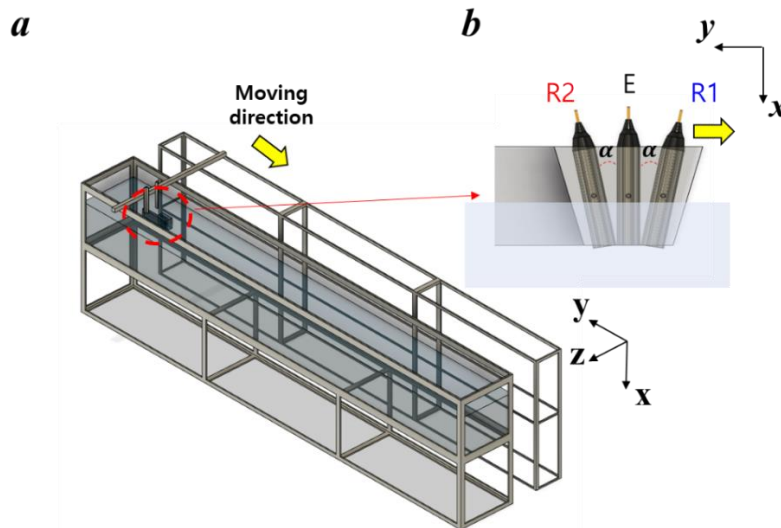
Fig. 4. Schematic of the experimental apparatus. (a) Towing tank facility and (b) transducer holder.

Feasibility tests were performed to evaluate the developed vector-UVP, and there were two purposes for these tests. One was to evaluate the relationships of the measurable distance and the inclining angle α (Section 3.1). The other was to estimate the results of the two-vector measurement (Section 3.2). For these tests, a 5-meter-long towing tank facility (LSA-N15HS-I-200S-4100-T2-X01-CT2, IAI Corp., Japan) was used with a transducer holder, as shown in Figs. 4 (a) and (b), respectively. The holder was fixed on the moving bar of the towing tank to measure the towed speed. Estimated speed fluctuation is approximately 1 % based on manufacturer-supplied data for this towed speed. As the towed speed was almost constant regardless of time, the flow condition is assumed to be a steady-state flow. Accordingly, the fluctuation of the measured velocity in time and space should converge to zero for this condition. In consideration of this, two tests were carried out.

For these tests, the tracer particles were mixed in water (HP 20SS, Mitsubishi Chemical). The density and diameter of the particles were 1010 kg/m³ and 50–120 μm, respectively. Regarding the experimental apparatus, not only the emitter but also the receivers consisted of TX4-5-8-40, which is a 4 MHz transducer, as mentioned previously. The emitter was driven by a pulser/receiver (JPR-600C, Japan Probe Co., Ltd.), and echo signals received from the transducers (E, R1, and R2) were amplified by preamplifiers (PR-60BP, Japan Probe Co., Ltd.) that included a band-pass filter function to improve the SNR. Their gain was maintained with +60 dB. The signals were digitized

and stored in an 8-bit data logger (DIG-100M1002-PIC, CONTEC) and transmitted to a PC hard disk.

3.1 *Feasibility test for the measurable distances in experiments*

An experiment was carried out to evaluate the measurable distances compared with the theoretical estimates (Table 3). As this test was not a feasibility test of the two-vector measurement, the transducer holder was installed horizontal to the water's surface (Fig. 4 (b)), and only the y-direction velocity (V_y) was measured. The experimental conditions are summarized in Table 4. Although $\alpha = 0°$ (Fig. 2 (a)) is beyond the scope of this study, we firstly present the experiment with $\alpha = 0°$ in order to discuss technical difficulties as explained in Section 2.1. Eq. (1) was used for $\alpha = 0°$ to obtain V_y, whereas Eq. (2) was used for the other angles.

Table 4. Experimental conditions for the validation test of the measurable distance.

Experimental conditions		
Ultrasound frequency (f_0)	4	MHz
Pulse repetition frequency (f_{PRF})	1	kHz
Cycles of ultrasound pulse	4	
Sound speed (c)	1480	m/s
Sampling speed	10	ns
Number of pulse repetitions	25	
Spatial resolution	0.74	mm
Measurement length	149	mm
Active diameter of the transducer (d_a)	5	mm
Number of velocity and echo intensity profiles	50	
Measurement time	5	s
Angles of receiver (α)	0, 5, 10, 15	degrees
Towed speed (V)	200	mm/s
Water temperature	21	°C

Concerning the result of V_y when $\alpha = 0°$, 50 velocity profiles of V_y were averaged, as shown in Fig. 5. The towed speed (V) was set as 200 mm/s while the measured V_y for each channel was approximately below 50 mm/s, which implies proper angle correction is required. The error bars indicate the standard deviation of V_y. In comparison with the later discussed proposed method, fluctuation is considerably higher against the average velocity. This was due to the low SNR issue at the receivers. Consequently, the configuration of the parallel transducers (Fig. 2 (a)) combined with the conventional transducer has several technical difficulties.
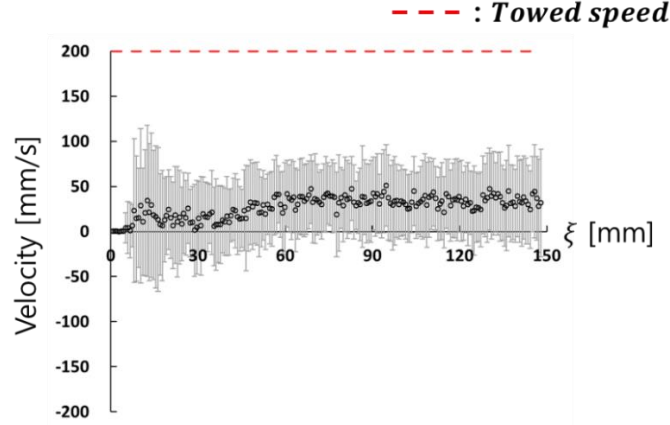
Fig. 5. Time-averaged V_y in $\alpha = 0°$. The error bar implies the standard deviation.
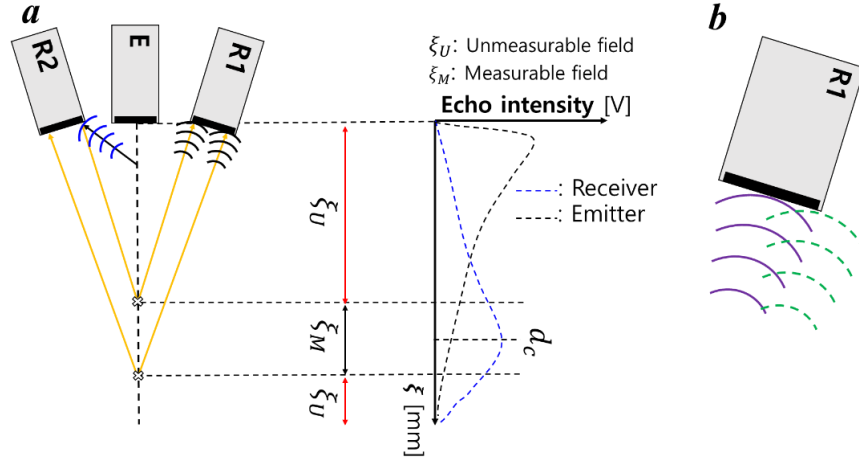

Fig. 6. A characteristic of the echo intensity in the configuration of the developed vector-UVP. (a) Echo intensity by the measurement distance and (b) ultrasound wave at the center (purple line) and margin (green dashed line) of the receiver.

Now, we discuss the proposed tilting arrangement. With regard to the feasibility test of the measurable distance, the distance could be evaluated using echo intensity and measured velocity. The echo intensity characteristics are illustrated in Fig. 6 (a). The intensity obtained at the emitter dropped along the measurement distance because of the attenuation of an ultrasound beam that occurred as a result of a divergence of the beam and absorption of acoustic energy [23]. Additionally, the echo intensity of the emitter was weak (incoherent) at the start point of the measurement distance because of the effect of the near-fields. Meanwhile, the ultrasound wave arrived more uniformly on the receiver surfaces in the measurable field (black waves illustrated in Fig. 6 (a)) than in the unmeasurable fields (blue wave illustrated in Fig. 6 (a)). As a result, the echo intensity sensed by the receiver increased when the measurement point approached the measurable distance, and then, the echo intensity by the measurement distance could be recognized, as in Fig. 6 (a). Consequently, the measurable field is determined by the acoustic fields of the emitter and the receiver. A peak of intensity should be at the center of the measurable field (d_c) because a larger amount of ultrasound energy arrived at d_c (purple line) than at the other detected point (green dashed line), as shown in Fig. 6 (b).

Considering this feature, the echo intensity at the receiver was calculated by the numerical simulation and then compared with the experiment when α was 5°, 10°, and 15°. The parameters of

numerical simulation are summarized in Table 5.

Table 5. Parameters for the numerical simulation.

Parameters of numerical simulation		
Ultrasound frequency (f_0)	4	MHz
Cycles of ultrasound pulse	2	
Sound speed (c)	1480	m/s
Sampling speed	10	ns
Attenuation coefficient (β)	0.01	1/mm
Spatial resolution	0.77	mm
Measurement length	150	mm
The distance between center of emitter and receiver (G)	9	mm
Active diameter of the transducer (d_a)	5	mm
Angles between the emitter and receiver (α)	5, 10, 15	degrees
Water temperature	21	°C

The attenuations of sound pressure (P_s) depend on the media and are expressed as

$$P_s = P_0 \exp(-\beta \xi_r),$$

where P_0, β and ξ_r mean the initial sound pressure, attenuation coefficient and round trip distance from the measurement point to the transducer. We omitted the reflection ratio induced by reflectors and the effect of near-field because the main purpose of the simulation is to estimate the changes of echo intensity in the measurable distance by the receiver angles.
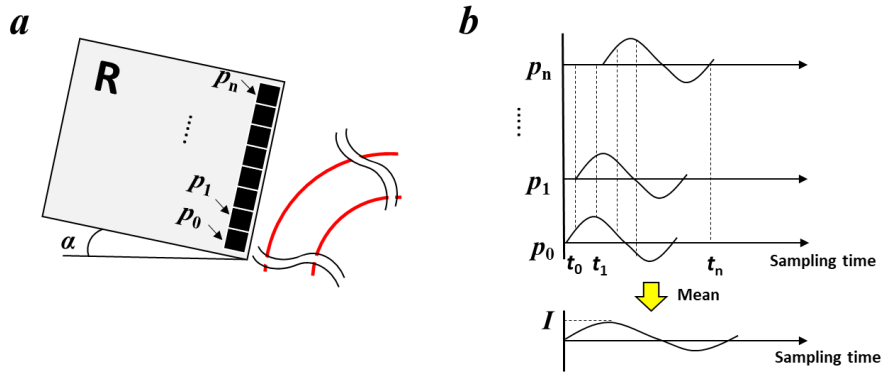

Fig. 7. Schematic diagram of the numerical simulation (a) 2D domain for the simulation, where p_n is detecting point on the receiver. (b) Time delay of signal detection for each detecting point.

A schematic of numerical simulation is described in Fig. 7. Since the ultrasound is received at each measurement point on the active diameter in regular sequence (Fig. 7(a)), the time delays for received echo signal exist as shown in Fig. 7(b). The echo signal is calculated by averaging the echo intensity for each sampling time. In this simulation, the representative echo intensity for each measurement channel was determined as the amplitude (I) of the averaged echo signal. The number of detecting points was 500, and the echo intensity of only one receiver was estimated because the receivers are symmetric as shown in Fig. 6(a).
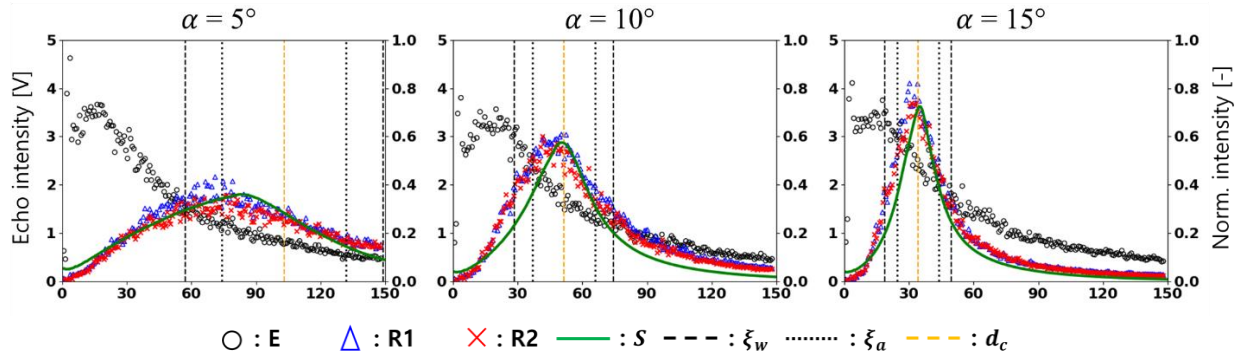
Fig. 8. Echo intensity distribution calculated by (a) numerical simulation and (b) experiment. E, R1, R2 and *S* mean the emitter, receiver 1, receiver 2 and numerical simulation, respectively.

The echo intensities calculated by the numerical simulation (*S*) and the experiment (E, R1 and R2) are shown in Fig. 8, respectively, where E is the emitter and R1 and R2 are the receivers depicted in Fig. 4. A horizontal axis indicates the measurement distance, and a left vertical axis and a right vertical axis indicate the echo intensity estimated from the experiment and the normalized echo intensity estimated from the numerical simulation, respectively. Dotted (ξ_a) and dashed lines (ξ_w) mean the measurable distance estimated by the active diameter and overall diameter, respectively, and the yellow dashed line means the center of the measurable field. The echo distributions of the simulation are slightly different to experiment results, and this is because we omitted the reflection ratio of reflectors and the near-field to simplify the simulation. However, the echo intensity obtained from the simulation and experiment shows almost the same trend for each α. The intensities of the receivers increased when the measurement point reached ξ_a in all α. Accordingly, it could be recognized that this result agreed with the idea that the ultrasound was more uniformly received on the receiver surface in the measurable distance than on the other points. Meanwhile, the peak point of intensity roughly existed in d_c with 10° and 15°, and the peak shifted to the left (near) side of ξ_a with 5°. This is attributed to a larger ultrasonic attenuation as the measurement distance increased. Because d_c was far away from the emitter in the case of 5°, the ultrasound energy at the receivers decreased when the measurement point approached d_c. From the figure, it was confirmed that the measurable distance is constructed well since received echo intensities are maintained within the measurable distances.
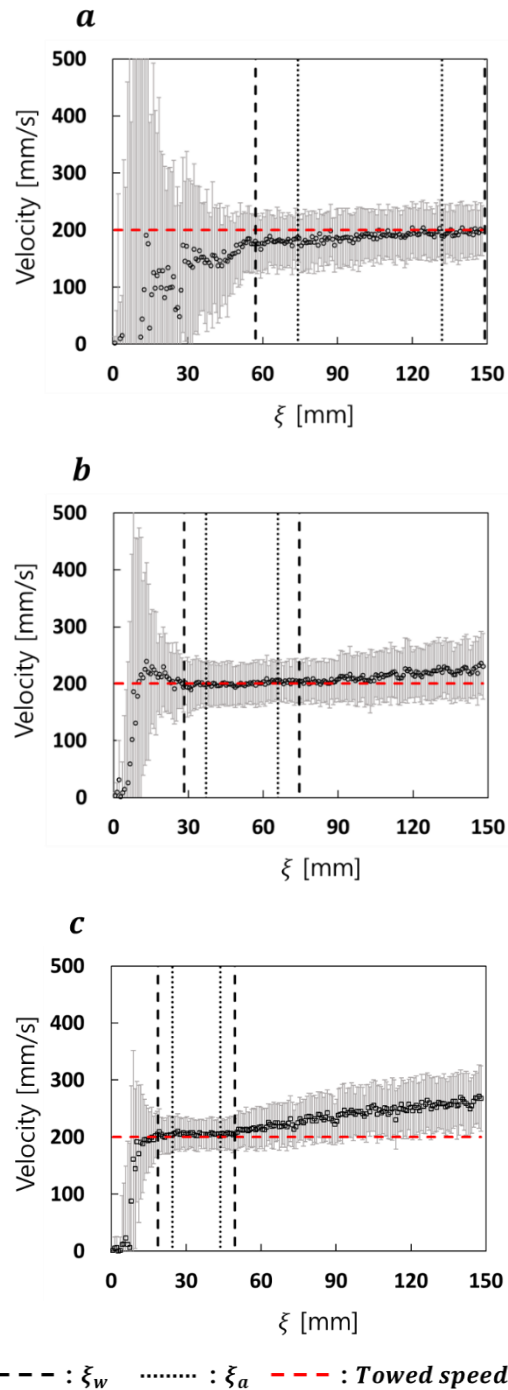
Fig. 9. Time-averaged V_y. (a) $\alpha = 5°$, (b) $\alpha = 10°$, and (c) α = 15°. The error bar implies standard deviation, and the red dashed line is the towed speed.

The time-averaged V_y values for the measured velocity in the measurable distance are shown in Fig. 9. In this result, the measured V_y converged to the towed speed V (red dashed line) in ξ_w and ξ_a whereas the measured velocity deviates and the standard deviations increase outside of ξ_w and ξ_a. In addition, V_y deviated from V at a far distance from ξ_w and ξ_a. This would be due to the acoustic field patterns and resulting uncertainty of the detected point at the receivers. At α of 5° (Fig. 9(a)), V_y shows gentle differences with V at starting points of ξ_w because of an incident angle of the ultrasound beam. The conventional transducers emit the ultrasound beam with straightness while the beam typically has a very small angle from the transducer body due to the transducer construction

13

tolerance. Although this angle does not have a great effect on normal measurements, it can cause minor errors when using with a low α. Since the sinusoidal value changes significantly at low angles, V_y can also change considerably as expressed in Eq. (2). If users want to obtain highly accurate measurements, it is recommended to perform calibration for the incident angle of the ultrasound. Note that calibration is not always required if certain errors can be acceptable. For example, overall tendency regarding the error between V_y and V at α of 10° and 15° (Fig. 9(b), (c)) has similarity within the measurable distance region because α is large enough to neglect the incident angle of the ultrasound beam. The spatiotemporal average error rates were within 3% in those α compared to V. Therefore, it can be said that the measurable distance is constructed well for each α. However, it is difficult to recognize which transducer diameter (d_a and d_w) is dominant in determining the measurable distance because the errors in ξ_w and ξ_a are equal regardless of α.

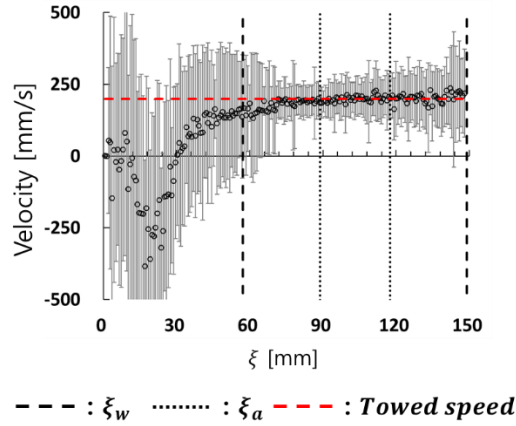− − − : ξ_w ········ : ξ_a − − − : *Towed speed*

Fig. 10. Time-averaged V_y with the 8MHz transducer (α = 5°). The error bar implies the standard deviation.

To clarify this point, an additional experiment was carried out using 8 MHz transducers (TX8-2.5-8-40) as the emitter and the receivers, and the ultrasound frequency was only changed to 8 MHz in the experimental conditions (Table 4). This 8 MHz transducer has the same d_w with the 4 MHz transducer while the active element of the 8 MHz transducer has a diameter of 2.5 mm and 4 MHz transducer has a diameter of 5 mm. Thus, d_g, defined in Fig. 3(b), became further away in the 8 MHz transducer than in the 4 MHz transducer, and then, the transferred ultrasound by oscillating a wear plate was reduced, as explained previously in Fig. 3 (b). For this reason, the measured V_y using the 8 MHz transducers had a higher standard deviation in ξ_w, as shown in Fig. 10. To be more specific, the time-averaged V_y converged to the towed speed not only in ξ_a but also in ξ_w. However, the standard deviation (σ_y) increased remarkably in ξ_w compared with ξ_a. The mean σ_y values in ξ_a and ξ_w obtained by the 4 and 8MHz transducers are summarized in Table 6.

Table 6. A comparison of mean σ_y values in ξ_a and ξ_w when using of 4 and 8MHz transducers, respectively.

	$\sigma_{y,4\text{ MHz}}$	$\sigma_{y,8\text{ MHz}}$
ξ_a	46.2 mm/s	71.2 mm/s
ξ_w	46.4 mm/s	103.9 mm/s
δ_σ	0.4%	31.5%

$$\delta_\sigma = \frac{\sigma_{y,\xi_w} - \sigma_{y,\xi_a}}{\sigma_{y,\xi_w}} \times 100 \ [\%] . \qquad (3)$$

There was a small difference of σ_y in ξ_a and ξ_w with the 4 MHz transducers, and the difference (δ_σ)

14

using Eq. (3) was 0.4%. By contrast, that of the 8 MHz transducers was 31.5%, which was much higher than that of the 4 MHz transducers. This was because d_g of the 4 MHz transducers was shorter than that of the 8 MHz transducers, as previously explained. σ_y could be considered an error in the instantaneous velocity profiles because this experiment was performed in the steady-state condition. That is, ξ_w could be adopted with the 4 MHz transducers, whereas ξ_a was more reasonable than ξ_w with the 8 MHz transducers. Accordingly, we could recognize that ξ_a could be adopted regardless of the transducer type. If it is necessary to use of wider measurable distance than ξ_a, we have to verify the accuracy before the use of a wide distance.

3.2 *Feasibility test for the calculation of two vectors in the experiments*
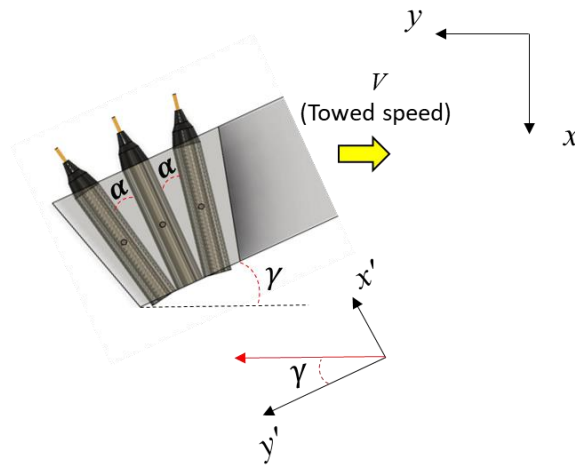

Fig. 11. A virtual coordinate by a tilting transducer holder.

The other feasibility test was conducted to evaluate the measurement of two vectors using the developed vector-UVP in the towing tank facility. To generate two vectors in the towing tank, the transducer holder was tilted with an angle γ, as shown in Fig. 11, and a virtual coordinate was formed with the x' and y' components. According to this coordinate, two-vector components, namely, $V_{x'}$ and $V_{y'}$, could be measured using the vector-UVP. Additionally, the velocity magnitude (V') remained constant regardless of γ because the towed speed was maintained as 200 mm/s in the experimental condition. Using this feature, the velocities in the x' and y' directions ($V_{x',\text{theo}}$ and $V_{y',\text{theo}}$) could be obtained theoretically using Eqs. (4) and (5), and this information could be considered the true value of the two vectors.

$$V_{x',\text{theo}} = V\sin\gamma, \qquad (4)$$
$$V_{y',\text{theo}} = V\cos\gamma. \qquad (5)$$

Three angles ($\gamma = 15°$, $30°$, and $45°$) were adopted in this test. Although V was not changed by γ, $V_{x',\text{theo}}$ and $V_{y',\text{theo}}$ were affected by γ, as shown in Table 7. On the basis of this information, the performance of the vector-UVP was evaluated by comparing $V_{x'}$ and $V_{y'}$ with $V_{x',\text{theo}}$ and $V_{y',\text{theo}}$, respectively.

Table 7. Theoretical $V_{x'}$ and $V_{y'}$.

	$\gamma = 15°$	$\gamma = 30°$	$\gamma = 45°$
$V_{x',\text{theo}}$ [mm/s]	52	100	141
$V_{y',\text{theo}}$ [mm/s]	193	173	141
V' [mm/s]	200	200	200

15

Compared to the experimental conditions in Table 4, f_{PRF} was changed from 1 to 2 kHz to suppress the aliasing problem encountered in the UVP system [23]. Furthermore, only α of 5° was adopted because it was confirmed that the measurable distance was constructed well in all α. Other than these two conditions, the other conditions were maintained in this test.

As the purpose of this test was to evaluate the accuracy of the two-vector measurement, it was essential to consider a velocity resolution. Although the velocity resolution in the receiver direction (ΔV_R) affected the resolution of $V_{x'}$ ($\Delta V_{x'}$) and $V_{y'}$ ($\Delta V_{y'}$), as shown in Eq. (6), it was difficult to calculate ΔV_R in the autocorrelation frequency analysis.

$$\Delta V_{x'} = \frac{\Delta V_R}{1 + \cos \alpha}, \quad \Delta V_{y'} = \frac{\Delta V_R}{\sin \alpha}. \qquad (6)$$

However, the resolution was roughly estimated using the denominator of the equation because the velocity resolution significantly depended on α. In this test, because $\alpha = 5°$ was adopted, the resolution could be estimated, as shown in Table 8. On the basis of the resolution, it could be recognized that the resolution of $\Delta V_{y'}$ was much higher than that of $\Delta V_{x'}$.

Table 8. Resolutions of each vector when $\alpha = 5°$.

	Velocity resolution
$\Delta V_{x'}$	$0.5\Delta V_R$
$\Delta V_{y'}$	$11.5\Delta V_R$

Fig. 12 shows the time-averaged $V_{x'}$ and $V_{y'}$ measured by the vector-UVP when γ was 15°, 30°, and 45°. The red dashed line indicates $V_{x',theo}$, and the yellow line indicates $V_{y',theo}$. It can clearly be recognized that $V_{x'}$ and $V_{y'}$ converge to the theoretical value in ξ_w in all γ conditions. The standard deviations of $V_{x'}$ are small, whereas $V_{y'}$ has standard deviations that are relatively larger. Accordingly, it can be thought that the instantaneous velocity of $V_{x'}$ converges to the theoretical value (i.e., $V_{x',theo}$), and $V_{y'}$ contains a slightly higher fluctuation in instantaneous velocity compared to $V_{y',theo}$. This results from a difference of velocity resolution in that $\Delta V_{x'}$ is approximately 23 times higher than $\Delta V_{y'}$. ΔV_y more strongly depends on α than $\Delta V_{x'}$, and in the case of lower α, ΔV_y deteriorates. Additionally, random noises can be included in the instantaneous velocity profiles because of the lack of velocity resolution. Thus, large tilting angle α is preferred to reduce the noises if a long measurement distance is not required.
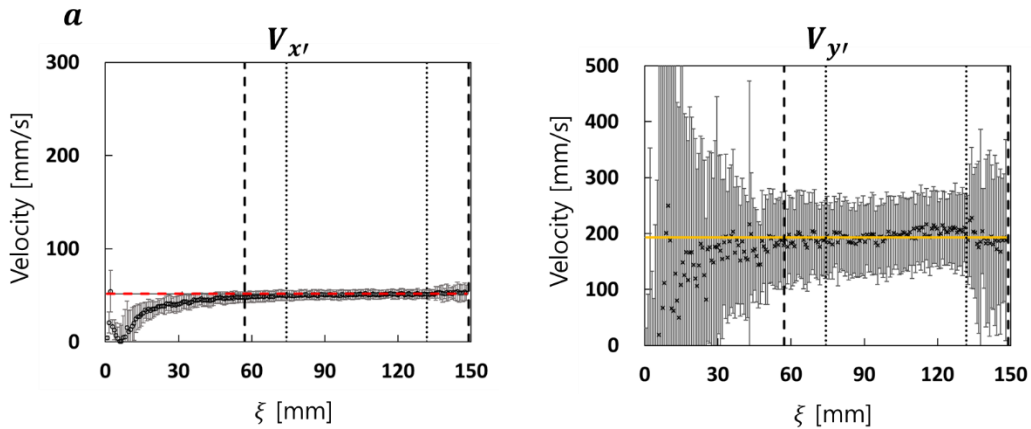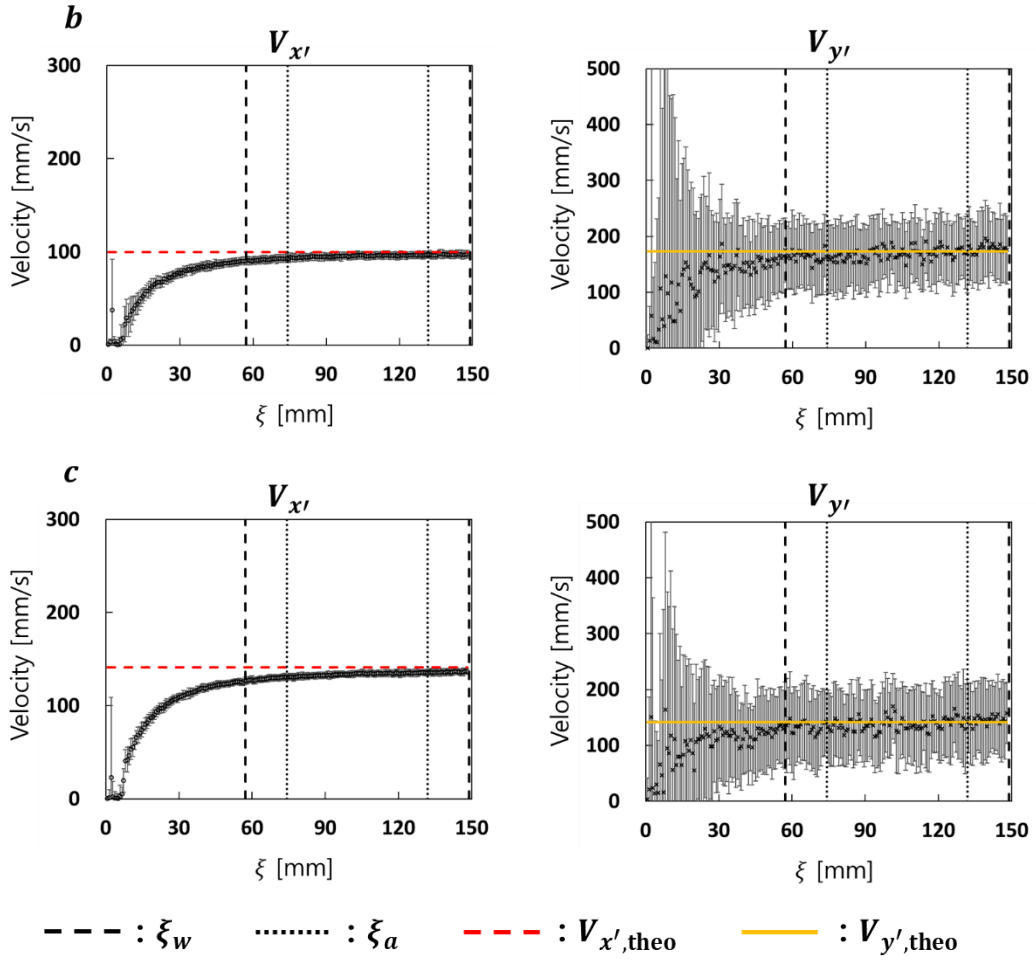
Fig. 12. Time-averaged $V_{x'}$ and $V_{y'}$. (a) $\gamma = 15°$, (b) $\gamma = 30°$, and (c) $\gamma = 45°$. The error bar implies the standard deviation, and the red dashed line and the yellow line represent $V_{x',\text{theo}}$ and $V_{y',\text{theo}}$, respectively.

Fig. 13 shows V' of the two vectors, and the spatiotemporal error (E_v) was obtained using Eq. (7).

$$E_v = \frac{|V - V'|}{V} \times 100 \, [\%], \quad V' = \sqrt{V_{x'}^2 + V_{y'}^2} \, . \qquad (7)$$

It can be seen that V' corresponds to the towed speed in ξ_a regardless of γ because the two vectors converge to the true value. The range of E_v was 1%–3% in ξ_a, as shown in Table 9. Thus, it is possible to say that the two vectors can be obtained with low errors using the vector-UVP in the time-average.
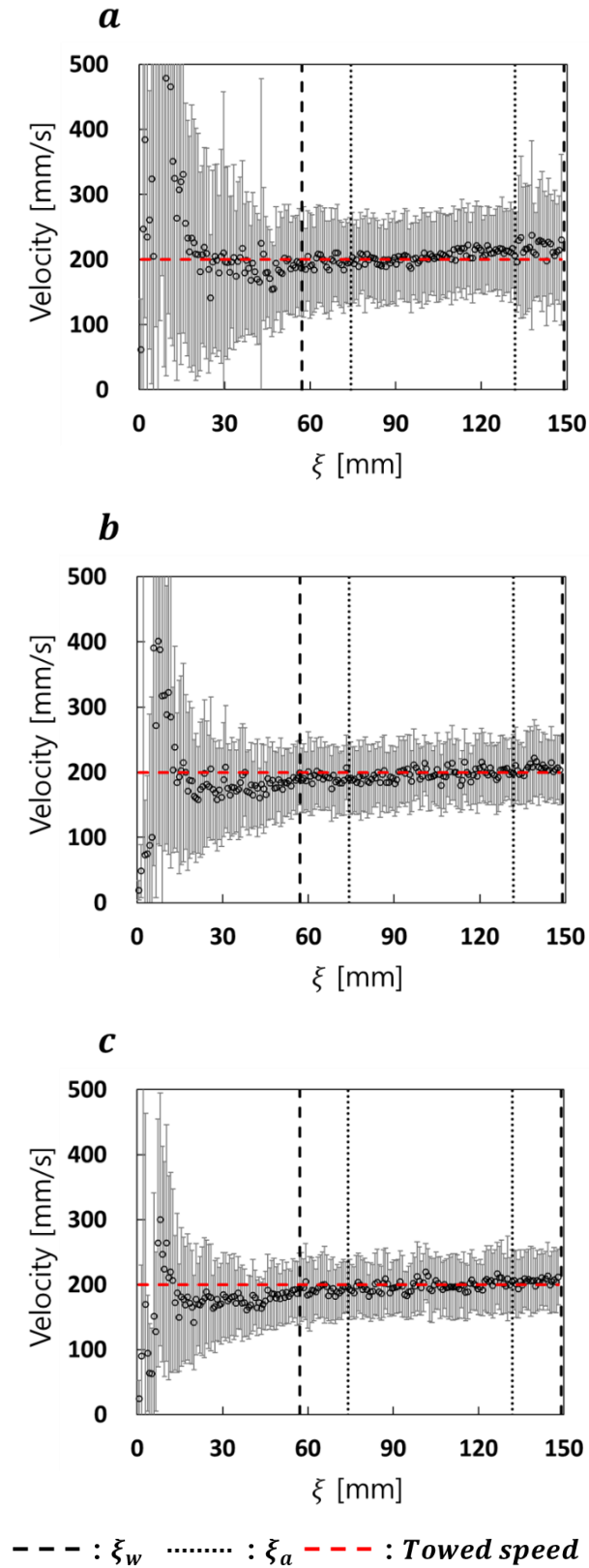
Fig. 13. Time-averaged *V′*. (a) *γ* = 15°, (b) *γ* = 30°, and (c) *γ* = 45°. The error bar implies the standard deviation, and the red dashed line is the towed speed.

18

Table 9. Spatiotemporal average error rate and standard deviation for each γ.

		$\gamma = 15°$	$\gamma = 30°$	$\gamma = 45°$
ξ_a	Mean σ_v [mm/s]	60	50	40
	Mean E_v [%]	3	2	1
ξ_w	Mean σ_v [mm/s]	70	50	50
	Mean E_v [%]	3	1	1

In previous studies for the vector-UVP, the maximal time-averaged error is within 4% using the focusing transducer [15], and flow rate error estimated by an element transducer is 5% [18]. Moreover, the time-averaged error range showed ± 15% using thin receivers [20]. Compared to these results, the proposed method is competitive because E_v in the measurable distance shows lower errors than the errors of other systems.

By contrast, the range of the standard deviations is 40–60 mm/s, being 20% and 30% of V, respectively. As the towed speed was constant, the standard deviation indicates the velocity estimation errors in the instantaneous velocity profiles. To evaluate the errors, the fluctuations of the instantaneous velocity in ξ_a were plotted in a quadrant graph for each γ, as shown in Fig. 14. The fluctuations of $V_{x'}$ and $V_{y'}$ (u' and v') were obtained using Eqs. (8) and (9), respectively. The horizontal axes signify the u' normalized by the standard deviation of $V_{x'}$ (u_{std}), and the vertical axes signify the v' normalized by the standard deviation of $V_{y'}$ (v_{std}).
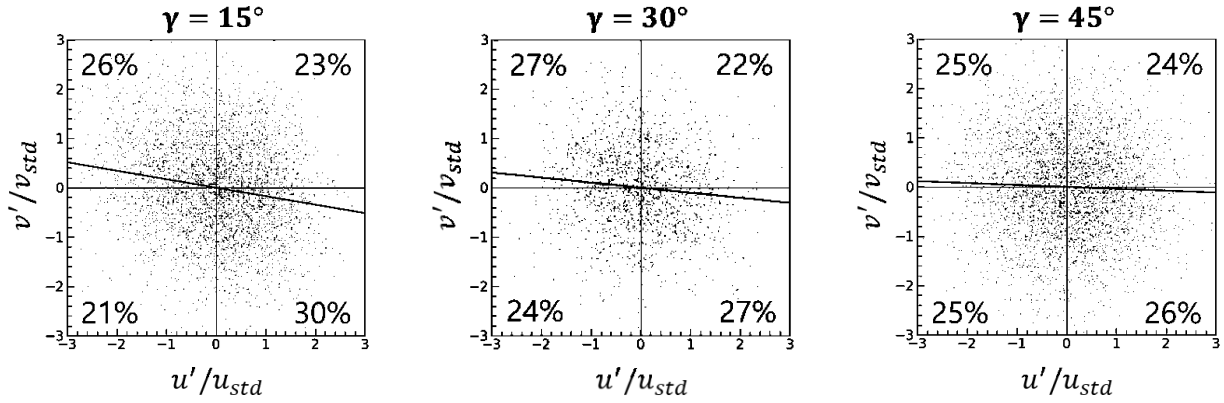

Fig. 14. Fluctuations of the instantaneous velocity in ξ_a when $\gamma = 15°$, 30°, and 45°. The horizontal axes are a normalized fluctuation of $V_{x'}$, and the vertical axes are a normalized fluctuation of $V_{y'}$. The black line signifies a trend line between the fluctuations for each vector.

$$u' = V_{x'} - \overline{V_{x'}}, \qquad (8)$$
$$v' = V_{y'} - \overline{V_{y'}} . \qquad (9)$$

The fluctuations are uniformly distributed in all quadrants in all γ and no bias is identified. It can be said that the error is due to random noises originating from the lack of velocity resolution. Therefore, α should be optimized to minimize the noises, in consideration of the measurement distance and the expected velocity ranges.

4. Demonstrations of the proposed vector-UVP

Two experiments were carried out as demonstrations of the developed vector-UVP. One experiment was to measure the Reynolds stress in a pipe flow. The Reynolds stress obtained from the vector-UVP was compared with the PIV. The other was a measurement of the vortex around a cylinder. A vortex-shedding frequency calculated from the experiment was compared with a theoretical equation.

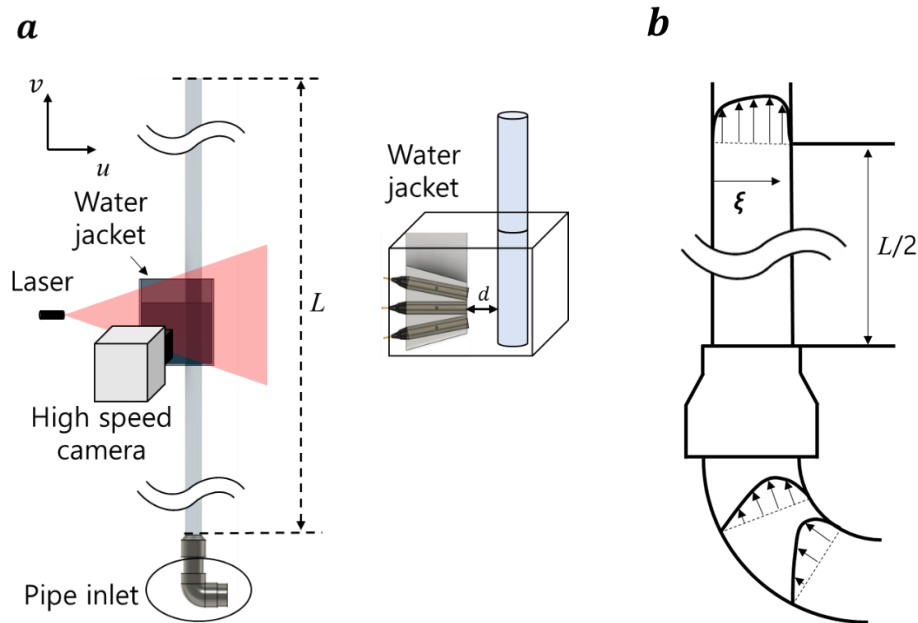## 4.1 *Measurement of the Reynolds stress in a pipe flow*

Fig. 15. Experimental equipment for the measurement of the Reynolds stress in a pipe flow. (a) a set-up of developed system in a water jacket, and (b) asymmetric velocity profile in the pipe induced by elbow socket.

A schematic diagram of the experimental equipment is shown in Fig. 15(a). An elbow socket is installed at the inlet of a pipe to the right as illustrated in the figure. The pressure gradient at an inner wall of the socket is negative, and this induces asymmetric flow in the pipe as shown in Fig. 15 (b) [24]. The experimental conditions are summarized in Table 10. The pipe has an inner diameter (D) of 50 mm and a length (L) of 2000 mm. As with the feasibility tests, HP 20SS was used as a tracer particle. The flow rate is measured using a flow meter (FT-0370, Showa Co., Ltd.). The Reynolds number defined by Eq. (10) was 50,000. In the equation, U_{bulk} is the bulk velocity of the liquid phase flow and v is a kinematic viscosity. The Reynolds stress was obtained in this turbulent pipe flow.

Table 10. Experimental conditions for the measurement of Reynolds stress in a pipe flow.

Experimental conditions		
UVP conditions		
Ultrasound frequency (f_0)	4	MHz
Pulse repetition frequency	2	kHz
Cycles of ultrasound pulse	4	
Sound speed (c)	1480	m/s
Number of pulse repetitions	27	
Spatial resolution	0.74	mm
Number of velocity profiles	500	
Measurement time	78	s
Angle of receiver (α)	5	degree
Distance between the emitter and pipe wall (d)	72	mm
PIV conditions		
Frame rate	1500	fps
Spatial resolution	0.9	mm
Measurement time	13	s
Flow conditions		
Pipe inner diameter (D)	50	mm
Flow rate	120	L/min
Bulk velocity (U_{bulk})	1000	mm/s
Reynolds number (Re)	50,000	
Water temperature	21	°C
Measurement point	L/2	

$$Re = \frac{U_{bulk}D}{v}. \qquad (10)$$

A measurement point of the vector-UVP and the PIV was matched at the center of L (L/2). As α = 5° allowed a measurement distance of more than 50 mm, α was determined as 5°. Considering one of the characteristics of the measurable distance in Table 3, the distance between the emitter and the inner wall of the pipe (d in Fig. 15) was set at 72 mm. Specifically, ξ_a was matched with D.

Five-hundred velocity profiles were obtained by the UVP, and the results are shown in Fig. 16. This shows the instantaneous velocity contours when the vertical axes represent the measurement time and the horizontal axes represent the measurement distance in the pipe with u and v components. The measurement distance is set from the left to the right side of the pipe as shown in Fig. 15 (b). In the v contour, the velocity was relatively low at the starting point of measurement, where the measurement distance was approximately 2 mm, compared with the velocity at the opposite wall. This was due to the multiple reflection that is widely known among UVP users.
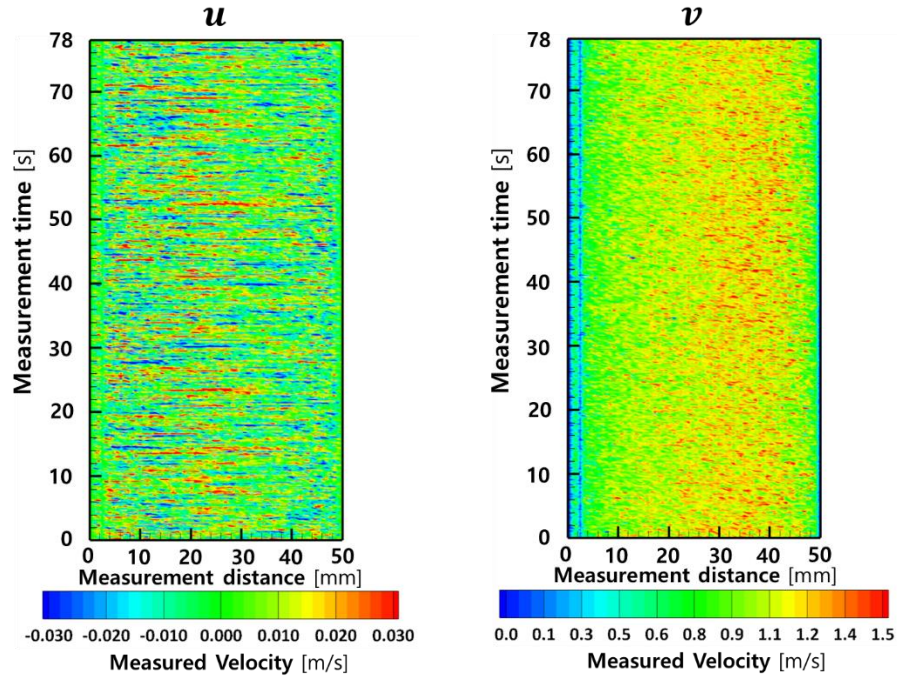
Fig. 16. Two-vector measurement in a pipe flow using the vector-UVP. Horizontal and vertical axes indicate measurement distance and time, respectively.
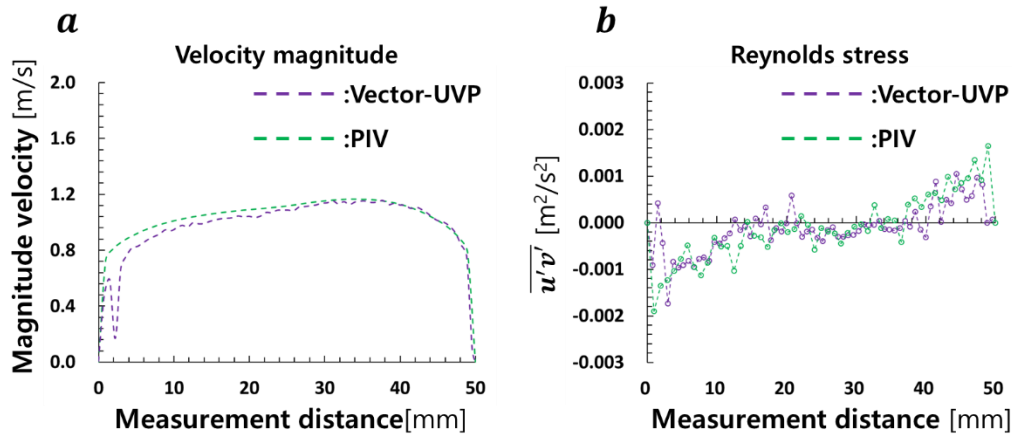

Fig. 17. A comparison of the UVP and PIV results. (a) The time-averaged velocity magnitude and (b) the Reynolds stress.

On the basis of these velocity profiles, the time-averaged velocity magnitude (Fig. 17 (a)) and the Reynolds stress (Fig. 17 (b)) were obtained by the vector-UVP (purple dashed line) and compared with the PIV (green dashed line). Because of the multiple reflection, the near wall velocities show erroneous data. Although there were small differences between the PIV and the vector-UVP up to a distance of 24 mm, the velocity distribution of the vector-UVP was almost the same with that of the PIV result. As explained previously, the velocity profiles by the vector-UVP and PIV were asymmetric because of the elbow socket connected with the pipe inlet. Traditionally, the Reynolds stress can be obtained from the velocity profiles on the multiple measurement lines of a UVP (not with a vector-UVP) by assuming that $\bar{u}$ becomes zero [25]. However, it is likely that $\bar{u}$ was not zero in this asymmetric flow. Consequently, the assumption used for the Reynolds stress estimation with the traditional UVP is not necessarily valid. Because the developed vector-UVP provides two vectors in the flow field, the Reynolds stress can be acquired in any flow condition. Regarding the measurement result of the Reynolds stress, small differences existed between the two

measurement results, but they agreed well with each other, except for the multiple reflection point. The Reynolds stress led to turbulent fluctuations in the fluid momentum, and the instantaneous velocity profiles were required to compute the stress. As the Reynolds stress obtained by the PIV and the vector-UVP was consistent, it could be said that the instantaneous velocities measured by the vector-UVP were statistically valid.

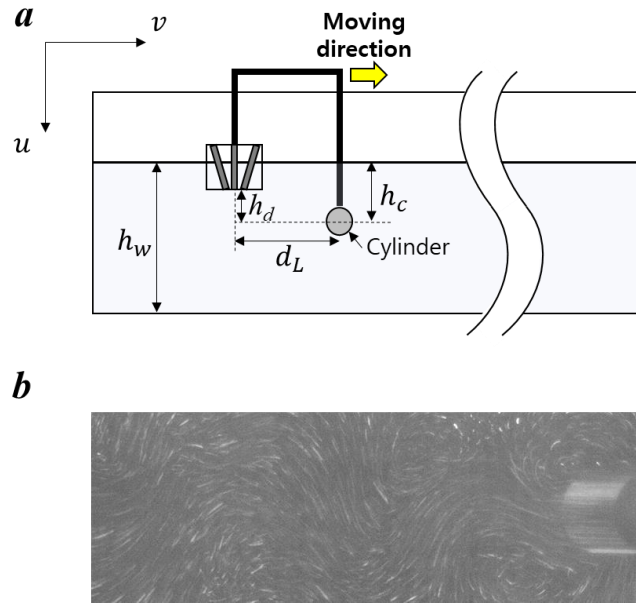## 4.2 *Measurement of vortex-shedding around a cylinder*

Fig. 18. Experimental setup for the measurement of a wake of a cylinder in a towing tank facility. (a) Experimental setup and (b) a snapshot of the wake.

Fig. 18 shows an experimental setup for the measurement of a wake around a cylinder in the towing tank facility and a snapshot of the wake around the cylinder. A cylinder with a diameter of 18 mm was installed. The transducers were mounted 30 mm behind the cylinder and were towed with the cylinder. The specific experimental conditions are summarized in Table 11.

Table 11. Experimental conditions for the measurement of the vortex around a cylinder.

Experimental conditions		
UVP conditions		
Ultrasound frequency (f_0)	4	MHz
Pulse repetition frequency	2	kHz
Cycles of ultrasound pulse	4	
Sound speed (c)	1415	m/s
Number of pulse repetitions	20	
Spatial resolution	0.7	mm
Time resolution	92	ms
Number of velocity profiles	109	
Measurement time	10	s
Angle of receiver (α)	10	degree
Flow conditions		
Towed speed (V)	50	mm/s
Water temperature	3	°C
h_w	255	mm

h_c	70	mm
d_L	30	mm
h_d	52	mm
Cylinder diameter (D)	18	mm
Re_D (Reynolds number)	850	
St (Strouhal number)	0.20	
f_v (vortex-shedding frequency)	0.56	Hz

As explained previously, the errors in the instantaneous velocity could be included because of the lack of velocity resolution. Thus, α of 10° was adopted in this experiment to increase the resolution. Additionally, it was confirmed that the measured velocity was valid in ξ_w, which was determined by the whole diameter of the 4MHz transducer. Thus, ξ_w was adopted as the measurement distance. In this experiment, the Reynolds number defined by Eq. (11) was 850.

$$Re_D = \frac{VD}{v}.$$ (11)

A theoretical vortex-shedding frequency was calculated to compare with the vortex frequency from the experiment using Eq. (12), where the Strouhal number (St) was 0.2 and the theoretical frequency was 0.56 Hz.
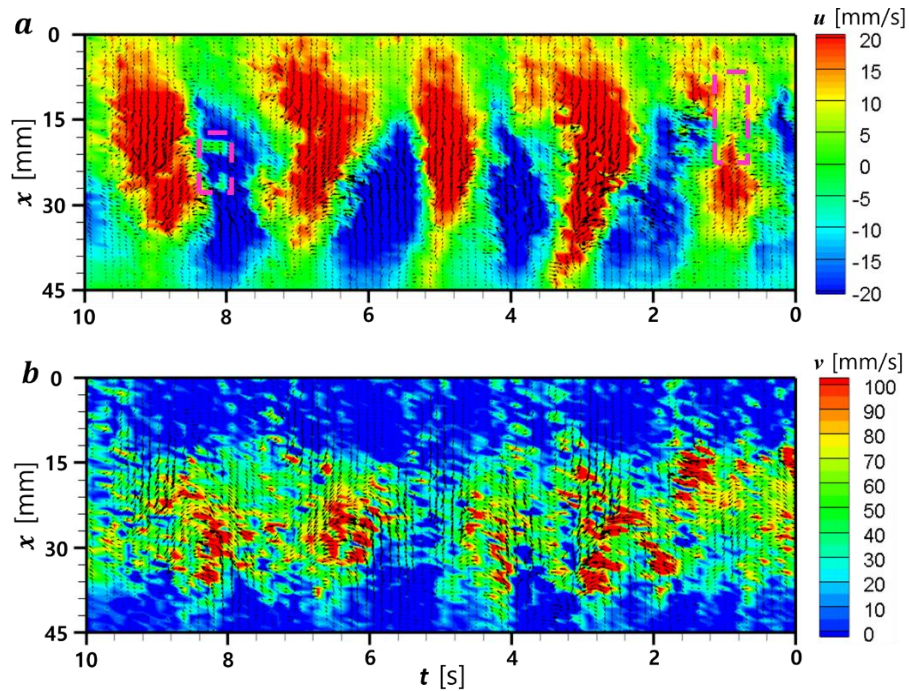
$$f_v = \frac{V}{DSt}.$$ (12)

Fig. 19. Instantaneous velocity vector profiles in (a) u vector and (b) v vector contour fields. The vertical axes mean the measurement distances, and the horizontal axes indicate the measurement times. Arrows indicate u and v vectors corresponding to each vortex, and these vectors are same for both contours.

Fig. 19 shows the temporal variation of the velocity profile in u vector and v vector contour fields, where arrows mean two vectors corresponding to each vortex. The horizontal axes are the measurement times arranged inversely (from left to right), vertical axes are the measurement

24

distances. The center of the cylinder was located at $x = 22.5$mm. In particular, the measured v vector is subtracted from the towed speed, and it is shown in Fig. 19 (b). Although it is difficult to observe small eddies using the UVP because of the lack of spatial resolution [26, 27], the five shedding vortexes, i.e., the large eddies, are observed periodically in Fig. 19 (a). However, the low-scale velocities close to zero, considered as errors, are observed in the pink-dashed squares. This is expected because of a local lack of particle density on the measurement distance when the cylinder is towed. Additionally, it was not able to show a clear vortex-vector field. There are two reasons for this: (1) the time resolution of the velocity profile (92 ms) is insufficient to observe the shedding vortex, and this problem was shown in the study conducted by Obayashi et al. [15]. (2) Errors resulting from the lack of velocity resolution are involved in this measurement system, and they have an effect on instantaneous velocity profiling. Thus, an interpolation can be required to observe the instantaneous velocity vector to remove the errors.

As the interpolation method, we adopted a low-pass filter based on a Fourier transform [28] because the shedding vortex was one of the periodical flows. The transform was conducted in a space–time domain of the vector-UVP data.
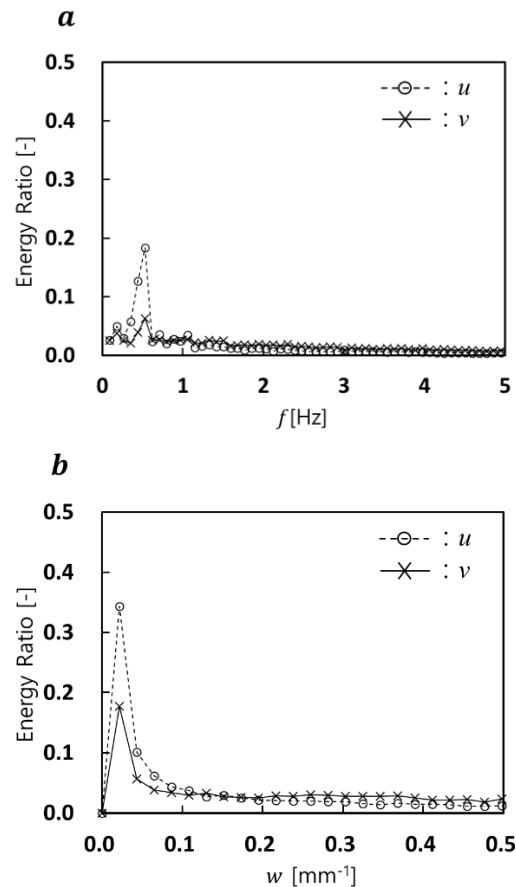

Fig. 20. Energy ratio of u and v vectors provided by the Fourier transform analysis in (a) time and (b) space domains.

Table 12. Cutoff frequency and wavenumber of the u and v vectors.

	Cutoff frequency	Cutoff wavenumber
u	1.4 Hz	0.20 mm^{-1}
v	2.7 Hz	0.40 mm^{-1}

Fig. 20 shows the energy spectrum ratio of u and v vectors in the (a) time and (b) space domains. As

shown in Fig. 20 (a), the energy ratio of u and v vectors peaks at 0.53 Hz, and this is in perfect agreement with the theoretical f_v. Accordingly, it can be said that the measurement result by the developed vector-UVP is reasonable. The cutoff frequency and the wavenumber of u and v vectors are determined when the summation of the energy ratio converges to 70%, and this is summarized in Table 12.
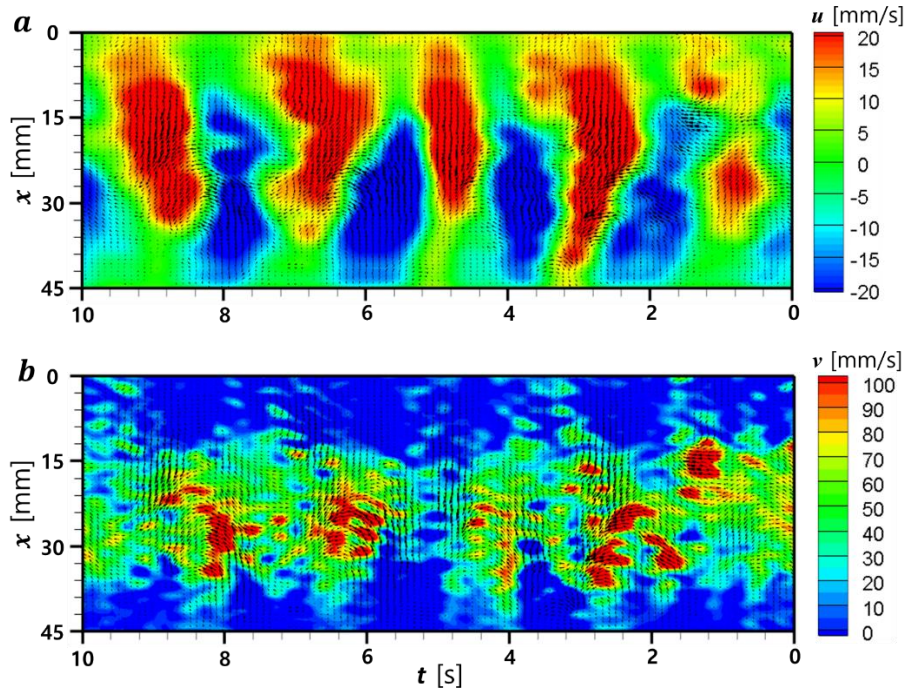

Fig. 21. Interpolated instantaneous velocity-vector profiles in (a) u vector and (b) v vector contour fields using a Fourier transform. The vertical axes mean the measurement distances, and the horizontal axes indicate the measurement times. Arrows indicate u and v vectors corresponding to each vortex, and these vectors are same for both contours.

The interpolated velocity vector fields, where arrows indicate u vector and v vector corresponding to the vortex, are shown in Fig. 21 after applying the low-pass filter on the original velocity field (Fig. 19). Although partial errors still remain in the vector fields, the contour fields and the vectors become smoother than the original result. As a whole, it is confirmed that the developed vector-UVP system can successfully reconstruct the instantaneous velocity vector field.

5. Conclusions

A method of profiling velocity vectors using a conventional ultrasound transducer was developed by minimizing the uncertainty of the detection point at the receivers. In the feasibility test for the measurement of the velocity vector, the spatiotemporal average error rates were within 3%. The Reynolds stress in a turbulent pipe flow and vortex shedding flow around a cylinder were measured by using the developed system, and the results showed good agreements with PIV and the theoretical shedding frequency, respectively.

Table 13. Comparison of the developed system with other studies for vector-UVP

	Availability	Time resolution	Accuracy	Measurement distance
Focusing TDX	Intermediate	High	High	Low
Phased array TDX	Low	Low	Intermediate	High
Element TDX	Low	High	High	High
Thin receiver	Low	High	Intermediate	High
This study	High	High	High	Intermediate

Here, we compare newly developed vector-UVP with other vector-UVP studies in four items; availability, time resolution, accuracy and measurement distance. The result is summarized in Table 13. The conventional transducers have been already supplied to many UVP users and therefore their availability is highest among all transducers. Of course, the focusing transducer is also one of commercial transducers, but it is not widely equipped in research and industry fields because of a fixed focusing distance. The others have the lowest availability since they require a new design to adopt for each measurement. The significant reduction of time resolution is inevitable with the phased array transducer while the other transducers show sufficient time resolutions with a comparison of common UVP. The accuracy was evaluated by comparing the previous studies [15, 16, 18, 20]. It showed error rates less than 20% when phased array transducer and thin receiver were adopted, whereas the rates were less than 10% with the other transducer. For the measurable distance, the developed system in this study involves a limitation of measurement distance caused by the tilting angle and sensor diameter of transducers. Considering the use of the basic frequency with $O(1$ MHz$)$ generally employed to UVP in the industrial fields, its distance is normally within few centimeters and is a sufficient length to measure flows in pipelines of the factory. Note that the focusing transducer offers the measurement distance only at the focused points and the others can measure in a distance with $O(10$ cm$)$ which depends on the attenuation of the echo intensity and the pulse repetition frequency. As a result, obviously, the developed system shows competitive performances. Various extended studies using this system will be discussed in the future.

Acknowledgments

References

[1] Y. Takeda, "Development of an ultrasound velocity profile monitor", *Nucl. Eng. Des.*, 1991, **126**:277–84.

[2]   O. Andreev, Y. Koiesnikov, A. Thess, "Application of the ultrasonic velocity profile method to the mapping of liquid metal flows under the influence of a non-uniform magnetic field", *Exp. Fluid*, 2009, **46**:77–83.

[3]   S. Franke, D. Rabiger, V. Galindo, Y. Zhang, S. Eckert, "Investigations of electrically driven liquid metal flows using an ultrasound Doppler flow mapping system", *Flow Measure. Instrum*., 2016, **48**:64–73.

[4]   M. Mori, Y. Takeda, T. Taishi, N. Furuichi, M. Aritomi, H. Kikura, "Development of a novel flow metering system using ultrasonic velocity profile measurement", *Exp. in Fluid*, 2002, **32**:153–160.

[5]   T. Yoshida, Y. Tasaka, H. J. Park, Y. Murai, H. Teramura, S. Koseki, "Inner structure visualization of fresh fruits utilizing ultrasonic velocity profiler", *J. Visualization*. 2018, **21**:253–265.

[6]   Y. Murai, Y. Tasaka, T. Nambu, Y. Takeda, S.R. Gonzalez, "Ultrasonic detection of moving interfaces in gas-liquid two-phase flow", *Flow Measure. Instrum*., 2010, **21**:356–366.

[7]   S. Wada, H. Kikura, M. Aritomi, "Pattern recognition and signal processing of ultrasonic echo signal on two-phase flow", *Flow Measure. Instrum*., 2006, **17**:207–224.

[8]   H.J. Park, Y. Tasaka, Y. Murai, "Ultrasonic pulse echography for bubbles traveling in the proximity of a wall", *Meas. Sci. Technol*., 2015, **26**:125301.

[9]   J. Hitomi, Y. Murai, H.J. Park, Y. Tasaka, "Ultrasound flow-monitoring and flow-metering of air-oil-water three-layer pipe flows", *IEEE Acess*, 2017, **5**:15021–15029.

[10] H. Murakawa, H. Kikura, M. Aritomi, "Application of ultrasonic doppler method for bubbly flow measurement using two ultrasonic frequencies", *Exp. Therm. Fluid Sci*., 2005, **29**:843–850.

[11] W. Liu, C. Tan, X. Dong, F. Dong, Y. Murai, "Dispersed oil–water two-phase flow measurement based on pulse-wave ultrasonic doppler coupled with electrical sensors", *IEEE Trans. Instrum. Meas*., 2018, **67** (9):2129–2142.

[12] S.Q. Wang, K.W. Xu, H.B. Kim, "Slug flow identification using ultrasound Doppler velocimetry", *Int. J. Heat Mass Transf*., 2019, **148**:119004.

[13] M.B. Azevedo, D. Santos, J.L.H Faccini, J. Su, "Experimental study of the falling film of liquid around a Taylor bubble", *Int. J. Multiphase flow*, 2017, **88**:133–141.

[14] D. Hurther, U. Lemmin, "A constant-beam-width transducer for 3D acoustic Doppler profile measurements in open channel flows", *Meas. Sci. Technol*., 1998, **9**:1706–1714.

[15] H. Obayashi, Y. Tasaka, S. Kon, Y. Takeda, "Velocity vector profile measurement using multiple ultrasonic transducers", *Flow Measure. Instrum.*, 2008, **19**:189–195.

[16] M. Batsaikhan, A. Hamdani, H. Kikura, "Visualisation of air–water bubbly column flow using array Ultrasonic Velocity Profiler", *Theor. Appl. Mech. Lett*., 2017, **6**:379–385.

[17] S. Shwin, A. Hamdani, H. Takahashi, H. Kikura, "Two-dimensional velocity measurement downstream of the double bend pipe using phased array ultrasonic velocity profiler", *Advance Exp. Mech.*, 2018, **3**:111–117.

[18] J.T. Owen, N. Shoji, A. Hamdani, T. Ihara, H. Takahashi and H. Kikura, "Design of new ultrasonic transducer with two elements for flow rate measurement using ultrasonic Doppler method*", E3S Web Conf.*, 2018, **43**:01011.

[19] J.T. Owen, N. Shoji, A. Hamdani, T. Ihara, H. Takahashi and H. Kikura, "Development of new ultrasonic transducer for multi-dimensional velocity profile measurement Using Ultrasonic Doppler Method", *11th International Symposium on Ultrasonic Doppler Method for Fluid Mechanics and Fluid Engineering*, 2018.

[20] W. Wongsaroj, J.T. Owen, H. Takahashi, N. THONG-UN and H. Kikura, "2D velocity vector profile measurement on bubbly flow using ultrasonic technique", *Mech. Eng. Journal*, 2020, **3**:19–00519.

[21] H. Murakawa, K. Sugimoto, N. Takenaka, "Effects of the number of pulse repetitions and noise on the velocity data from the ultrasonic pulsed Doppler method with different algorithms", *Flow Measure. Instrum.*, 2014, **40**:9–18.

[22] C. Kasai, K. Namekawa, A. Koyano, R. Omoto, "Real-time two-dimensional blood flow imaging using an autocorrelation technique", *IEEE Trans Sonics Ultrasonics*, 1985, SU-**32**:458–64.

[23] Y. Takeda, "Ultrasonic Doppler Velocity Profiler for Fluid Flow", Ser. 101, Springer, Berlin, 2014.

[24] A. Ono, N. Kimuram H. Kamide and A. Tobita, "Influence of elbow curvature on flow structure at elbow outlet under high Reynolds number condition", *Nucl. Eng. Des*., 2011, **241**:4409–4419.

[25] H. Murakawa, H. Kikura, M. Aritomi, "Measurement of Reynolds stress in bubbly flow using ultrasound doppler method", *3rd International Symposium on Ultrasonic Doppler Method for Fluid Mechanics and Fluid Engineering*, 2002

[26] T. Taishi, H. Kikura, M. Aritomi, "Effect of the measurement volume in turbulent pipe flow measurement by the ultrasonic velocity profile method (mean velocity profile and Reynolds stress measurement). *Exp. Fluids*, 2002, **32**:188–196.

[27] H.J. Park, Y. Tasaka, Y. Oishi, Y. Murai, "Drag reduction promoted by repetitive bubble injection in turbulent channel flows", *Int. J. Multiphase flow*, 2015, **75**:12–25.

[28] N. Tiwari, Y. Tasaka, Y. Murai, "Pressure field estimation from ultrasound Doppler velocity profiler for vortex-shedding flows", *Flow Measure. Instrum.*, 2019, **67**:23–32.